Applied Catalysis A, General 571 (2019) 61–70

Contents lists available at ScienceDirect

Applied Catalysis A, General

journal homepage: www.elsevier.com/locate/apcata

Effect of Co incorporation and support selection on deoxygenation selectivity and stability of (Co)Mo catalysts in anisole HDO

Chanakya Ranga[a], Vaios I. Alexiadis[a], Jeroen Lauwaert[b], Rune Lødeng[c], Joris W. Thybaut[a,*]

[a] Laboratory for Chemical Technology, Ghent University, Technologiepark 914, B-9052, Ghent, Belgium
[b] Industrial Catalysis and Adsorption Technology, Ghent University, Valentin Vaerwyckweg 1, B-9000, Ghent, Belgium
[c] SINTEF Materials and Chemistry, Kinetics and Catalysis research team, N-7465, Trondheim, Norway

ARTICLE INFO

Keywords:
Bio-oil
Hydrodeoxygenation
Anisole
CoMo
Titania
Alumina
Zirconia

ABSTRACT

A series of supported Co modified Mo catalysts was prepared by varying the Co/Mo ratio in the range from 0 to 1 while maintaining the Mo loading at ca. 10 wt%. A sequential incipient wetness impregnation method, with Mo being introduced first, using aqueous solutions of the corresponding precursor salts was employed during the synthesis procedure. Three supports, i.e., Al_2O_3, ZrO_2, and TiO_2 differing in textural and acidic properties were investigated. Material physicochemical characteristics were evaluated through ICP-OES, N_2-sorption, XRD, H_2-TPR, NH_3-TPD, O_2-TPO, STEM-EDX and XPS techniques. The anisole HDO performance of these CoMo catalysts was evaluated at gas phase conditions in a fixed bed tubular reactor in plug flow regime. The catalysts performance is correlated with properties such as reducibility, acidity, and metal-support interactions. Cobalt addition enhanced the total HDO selectivity by 45% as compared to Mo catalysts. Alumina catalysts displayed higher initial activity ($X_{anisole} \approx 97\%$) relative to titania and zirconia supported variants ($X_{anisole} < 40\%$) at identical operating conditions. Titania supported catalysts exhibited rather higher stability compared to zirconia and alumina catalysts over 50 h time on stream (TOS), while zirconia catalysts displayed the highest HDO selectivity (up to 86%). Characterization studies of pre and post-reaction catalysts indicate Mo^{5+} to be the main active phase while over-reduction to lower Mo states (Mo^{4+} and Mo^{3+}) as well as carbon deposition are identified as the cause for catalyst activity decrease with TOS.

1. Introduction

The high consumption of fossil fuels and corresponding environmental impact continue to spark interest in finding cleaner-energy sources. Lignocellulosic biomass processing through various thermochemical techniques, e.g., fast pyrolysis, leading to biooils, is a very promising alternative [1–3]. One of the most important research areas in biooil valorization is catalytic hydrodeoxygenation (HDO) during which fuels or suitable blending agents including aromatic and aliphatic hydrocarbons such as benzene, toluene, and cycloalkanes are produced [4].

The complexity of lignin and, hence, of the correspondingly obtained fast pyrolysis oil, has prompted the use of model compounds such as phenolics, furans, ethers, acids etc. to study the intricacies of the hydrodeoxygenation reactions. Among the oxygenates in biooil, phenolics constitute about one fourth and are the most refractory to HDO [5,6]. Alkoxy groups are among the majorly occurring moieties within ligninderived phenolics [6,7]. Anisole, because of its methoxy group, has already been widely investigated as a model compound for lignin derived biooil [8–13]. The direct deoxygenation of anisole, i.e., breaking the $C_{aromatic}$ −O bond rather than the $C_{aliphatic}$ −O bond poses a specific challenge as the former bond energy exceeds that of the latter by 84 kJ mol^{-1} [6]. Moreover, deoxygenation catalyst development aims at selective oxygen removal rather than aromatic ring hydrogenation for minimizing the hydrogen consumption as well as to maintain an appropriate aromatic content [7,14,15].

The low sulfur content in biooil renders the use of traditional, sulfided catalysts such as NiMoS and CoMoS less interesting. Such catalysts require a tailored amount of sulfur in the processed feeds to maintain their activity and selectivity and, hence, end products are inevitably contaminated by sulfur [16–19]. To mitigate this issue, non-sulfided transition metal (Ni, Co, Mo) catalysts on various supports have been investigated for hydrotreatment of biooil model compounds [20–22]. Yet, significant challenges remain to improve the catalyst activity, stability, and HDO selectivity.

Another type of catalysts which are interesting for HDO reaction are

* Corresponding author.
E-mail address: Joris.Thybaut@UGent.be (J.W. Thybaut).

https://doi.org/10.1016/j.apcata.2018.12.004
Received 25 June 2018; Received in revised form 4 December 2018; Accepted 7 December 2018
Available online 07 December 2018

those based on noble metals [23–26]. Noble metals generally exhibit good HDO activity but are mostly selective towards aromatic ring hydrogenation rather than deoxygenation. This leads to higher hydrogen consumptions at pressures ranging from atmospheric pressure to 4 MPa [25–28]. Even though exhibiting promising results, noble metals have their excessive price and limited availability as major disadvantages. This renders processes employing them economically less feasible. To remediate this issue, various non-noble transition metals have recently been developed for bio oil HDO, among which Mo-based catalysts, that have exhibited excellent activity and selectivity towards targeted deoxygenation reactions [12,13,29].

Our previous work on zirconia supported MoO_3 catalysts has led to adequate activities and stabilities, while the HDO selectivity did not exceed 50% [30]. Several supported metal-Mo catalyst compositions have already been tested under HDO conditions and among the promoter metals (including noble metals such as Pd, Pt, Re), Co has been found to induce one of the highest hydrodeoxygenation to aromatic ring hydrogenation ratios [4,19,31]. On supported Mo and CoMo catalysts, interactions between the metal (oxide) and the support have been reported to determine the exact structure of this metal oxide, which can affect reducibility, catalytic activity as well as total acidity of the catalyst materials [21,29,32–37].

In the present work, the effect of the Co/Mo ratio and the type of support of Co-Mo materials on their HDO performance has been investigated. In particular, three supports, i.e., ZrO_2, Al_2O_3, and TiO_2, exhibiting different textural and acidic properties are probed. The impact of metal and support properties, i.e., reducibility and acidity, as well as of metal-support interactions on the catalysts activity, stability and selectivity under HDO experimental conditions is presented.

2. Experimental methods

2.1. Catalyst preparation

A series of supported Co modified Mo catalysts was prepared by varying the Co/Mo ratio in the range from 0 to 1 while maintaining the Mo loading at ca. 10 wt%. A sequential incipient wetness impregnation method using aqueous solutions of the corresponding precursor salts, i.e., ammonium heptamolybdate ($(NH_4)_6Mo_7O_{24}.4H_2O$, Alfa Aesar) and cobalt nitrate hexahydrate ($CoN_2O_6.6H_2O$, Alfa Aesar), was employed, with the former being introduced first. Support pellets were first crushed and sieved to obtain the 100–300 µm particle size fraction, and were subsequently calcined at 500 °C for 5 h prior to impregnation. After the impregnation of Mo salt on to the support, the samples were dried at room temperature for 12 h and then at 120 °C for 24 h, followed by calcination under flowing air (ca. 150 ml min^{-1}) at 550 °C for 6 h. Subsequently, Co salt was impregnated with same post impregnation steps as that of Mo impregnation. Three different supports, i.e., Al_2O_3, ZrO_2 and TiO_2 (Alfa Aesar), were used. The resulting calcined materials were designated as (xCo)MoA, (xCo)MoZ, and (xCo)MoT respectively, where "x" refers to the corresponding Co/Mo ratio present in the material.

2.2. Catalyst characterization

N_2 adsorption–desorption isotherms of the powdered catalyst samples were measured at −196 °C using a Micromeritics TriStar II 3020 instrument. The specific surface area (S_{BET}) was calculated by the Brunauer–Emmett–Teller (BET) method. The average pore volume was obtained using the Barrett–Joyner–Halenda (BJH) method. Prior to these measurements, the samples were outgassed at 200 °C for 2 h to remove any volatile adsorbates from the surface.

The bulk elemental composition of as-prepared catalysts was determined by means of inductively coupled plasma optical emission spectroscopy (ICP-OES, ICAP 6500, Thermo Scientific). The samples were mineralized by alkaline fusion with sodium peroxide.

An AutoChem 2920 instrument with a thermal conductivity detector (TCD) was applied for the temperature programmed reduction using hydrogen, i.e., H_2-TPR. Sample amounts of ca. 100 mg were loaded in a U-shaped tubular quartz reactor, with an internal thermocouple positioned at the level of the sample bed. Prior to H_2-TPR, the sample was purged with high purity (99.999%) Argon (60 ml min^{-1}) at 200 °C for 2 h. To obtain the TPR profiles the temperature was progressively increased from ambient to 900 °C at a rate of 10 °C min^{-1} in a mixture of 10 vol.% H_2/Ar.

Acidity measurements were performed by temperature programmed desorption with NH_3 (NH_3-TPD), also on the AutoChem 2920 instrument coupled with a TCD. Prior to NH_3-TPD, the sample was purged with high purity (99.999%) helium (60 ml min^{-1}) at 200 °C for 2 h. After pretreatment, the sample was saturated with high purity anhydrous ammonia employing 4 vol.% NH_3/He (75 ml min^{-1}) at 80 °C for 2 h and subsequently flushed at 110 °C for 1 h to remove physisorbed ammonia. The TPD analysis was carried out from ambient temperature to 700 °C at a heating rate of 10 °C min^{-1}. A calibration factor was determined by calibrating the detector with known volumes of NH_3 [38]. The amount of ammonia desorbed was correlated to the area under the TPD curve.

Temperature programmed oxidation experiments using oxygen (O_2-TPO) were also conducted on the AutoChem 2920 instrument. The outlet gas stream was monitored online using a calibrated OmniStar Pfeiffer mass spectrometer (MS). In a typical TPO experiment, the spent catalyst sample was purged with high purity (99.999%) helium (60 ml min^{-1}) at 200 °C for 2 h followed by heating from ambient temperature to 700 °C under 10 vol% O_2/He (45 ml min^{-1}). The heating rate used for O_2-TPO was 10 °C min^{-1}. For quantification, the MS is focused to different amu signals, the selection of which was based on the analysis of the mass spectra of the individual components. The CO_2 signal was monitored at $m/z = 44$, that of CO at 28, that of He at 2, and that of O_2 at 16. The amount of carbonaceous species was quantified by calculating the evolved CO_2 during a typical TPO experiment. The CO signal observed to be negligible during the present experiments and any CO produced probably converted to CO_2.

X-Ray Diffraction (XRD) patterns of the powdered catalyst samples were recorded at room temperature on a Siemens Diffractometer Kristalloflex D5000, using Cu Kα radiation (λ = 1.54 Å). The X-ray tube voltage was set to 40 kV and the current to 50 mA. XRD patterns were collected in the range of 2θ from 10° to 90° with a step size of 0.02°.

Xray Photoelectron Spectroscopy (XPS) analysis was performed under ultrahigh vacuum conditions using an Axis Ultra DLD XP spectrometer from Kratos Analytical and monochromatic Al Kα radiation ($h\nu$ = 1486.6 eV). A pass energy of 160 eV was used for survey scans and 20/40 eV was used for the individual core levels. Charge compensation using low energy electrons was applied during acquisition. The binding energy scales were calibrated to the adventitious carbon of C1s component at 284.6 eV. The background was subtracted using a Shirley function and the spectra were fitted using a convolution of Gaussian and Lorentzian functions. The composition of Mo oxidation states was estimated by the deconvolution of Mo 3d doublet. The following constraints were used for deconvolution: (1) Splitting energy of 3.2 eV for Mo $3d_{5/2}$–Mo $3d_{3/2}$, (2) Area intensity ratio of 3:2 for Mo $3d_{5/2}$–Mo $3d_{3/2}$, and (3) Equal full width at half maximum (FWHM) of Mo $3d_{5/2}$ and Mo $3d_{3/2}$ [30]. Mo $3d_{5/2}$ and $3d_{3/2}$ components are located at 232.55 and 235.7 eV respectively [39–41].

Scanning Transmission Electron Microscopy (STEM) was used for structural analysis, while EDX yielded local elemental mapping. These techniques were performed using a JEOL JEM-2200FS, Cs-corrected microscope operated at 200 kV, which was equipped with a Schottky-type field-emission gun, FEG, and EDX JEOL JED-2300D. All samples were deposited by immersion onto a lacey carbon film on a copper support grid.

Table 1
Overview of the range of performance test conditions.

Operating condition	Experimental range
Catalyst pellet diameter (μm)	100–200
Temperature (°C)	340
Total pressure (MPa)	0.5
Space time (kg_{cat} s $mol_{anisole}^{-1}$)	5–230
H_2/anisole (mol_{H2} $mol_{anisole}^{-1}$)	50

2.3. Catalyst activity measurements

2.3.1. Experimental setup and operating conditions

Kinetic experiments for gas phase anisole HDO were carried out in a state of the art high throughput kinetic screening setup, HTKS [42]. A schematic representation of the setup is provided in SI Fig. 1 and a more elaborate description can be found in our previous work [30]. It comprises 16 parallel reactors (L = 85 cm, i.d. = 0.21 cm), in which catalyst particles with size 100–200 μm are loaded, diluted with α-alumina inert of the same size, between two inert α-alumina layers. The inert layer on top of the catalyst bed ensures complete liquid feed vaporization and adequate mixing, as well as the development of the plug flow regime before the reacting fluid reaches the catalyst bed. Hydrogen diluted with helium was used as gas feed and anisole dissolved in n-hexane with n-octane as internal standard, as the liquid feed. The absence of heat and mass transport limitations and the establishment of the ideal plug flow regime were verified via adequate correlations, see SI Table 1 [43]. The investigated range of the operating conditions is presented in Table 1. The product stream was analyzed with an on-line gas chromatograph, i.e., a DHA (Detailed Hydrocarbon Analyzer) TraceGC1310 equipped with 2 flame ionization detectors (FIDs, front and back). For the present analysis, the Front FID with a Rtx-PONA column (L = 100 m, i.d. = 0.25 mm) was used.

Prior to the kinetics measurements, the catalyst was activated in situ by drying first at 200 °C for 2 h under helium and subsequently by reduction under H_2/He (70% v/v) till 500 °C at 5 °C min^{-1}. The catalyst was maintained at that temperature for 3 h at a total pressure of 0.5 MPa.

2.3.2. Data treatment

The conversion of feed component k, X_k, is defined on a molar basis as shown in Eq. (1),

$$X_k = \frac{F_k^0 - F_k}{F_k^0} \quad (1)$$

F_k^0 and F_k represent the inlet and outlet molar flow rates of component k. The selectivity, Sel_i, for product i coming from the feed component k is calculated using Eq. (2) on an elemental carbon basis, where cn_i is the number of carbon atoms in molecule i.

$$Sel_i = \frac{cn_i F_i}{cn_k (F_k^0 - F_k)} \quad (2)$$

The selectivity towards hydrodeoxygenation products, S_{HDO}, is given by Eq. (3).

$$S_{HDO} = \frac{\sum_{i=1}^{nHDO} cn_i F_{i,HDO}}{cn_k (F_k^0 - F_k)} \quad (3)$$

$F_{i,HDO}$ represents the outlet molar flow rate of hydrodeoxygenated product i and n_{HDO} represents the total number of deoxygenated products, created from feed component k.

3. Results and discussion

3.1. Material characterization

3.1.1. Textural properties and elemental composition

The metal loading and specific surface area (S_{BET}) of the materials obtained through ICP analysis and BET measurements respectively are reported in Table 2 and SI Table 2. As can be seen, S_{BET} decreases with increasing metal loading, i.e., initially with Mo and subsequently with Co introduction in the catalyst, which is attributed to the gradual filling of the pore volume [30,44,45]. All metal loaded samples exhibit lower surface area and pore volume compared to the pure support (see SI Fig. 2).

3.1.2. Structural composition

X-ray diffraction analyses of pure and metal loaded supports are given in Fig. 1. As can be seen, the most prominent crystalline phases identified in the metal loaded samples are pure MoO_3, and Co_3O_4 as well as a mixed $CoMoO_4$. The monometallic Mo-supported material MoA presents sharper peaks, characteristic of MoO_3 phase, than MoZ, while MoT does not present such peaks. This can be attributed to the different Mo-support interactions, which, particularly in the case of MoT, appear to result in more amorphous or highly dispersed MoO_3 onto the support. Interestingly, the incorporation of Co in the MoT sample results in the aggregation of the MoO_3 phase, i.e., the MoO_3 peak in the XRD pattern is becoming more pronounced. In the case of the other two monometallic Mo-supported samples, MoO_3 dispersion seems to be promoted by incorporation of Co, as derived from the reduction of the MoO_3 peak height. With increasing Co loading, peaks characteristic of Co_3O_4 and $CoMoO_4$ phases become sharper in the case of MoZ and MoA, yet these phases are highly dispersed and/or rather

Table 2
Catalyst and support properties.

Material	S_{BET} (m^2 g^{-1})	Co (Wt.%)	H_2 uptake (μmol g^{-1})			NH_3 uptake		metal/acid site ratio[a]
			Region I	Region II	Total	(μmol g^{-1})	(μmol m^{-2})	(-)
ZrO_2	99 ± 1	–	–	–	–	432	4.4	–
MoZ	80 ± 2	–	67	120	187	356	4.5	0.5
0.25CoMoZ	80 ± 4	2.2 ± 0.1	40	131	172	306	3.8	0.6
0.6CoMoZ	67 ± 4	5.8 ± 0.1	73	189	262	237	3.5	1.1
1CoMoZ	66 ± 4	8.9 ± 0.2	50	111	161	207	3.2	0.8
Al_2O_3	225 ± 10	–	–	–	–	1112	4.9	–
MoA	220 ± 1	–	65	141	205	980	4.5	0.2
0.25CoMoA	206 ± 4	2.8 ± 0.1	43	189	231	955	4.6	0.2
0.6CoMoA	193 ± 10	6.1 ± 0.1	42	204	246	895	4.6	0.3
1CoMoA	181 ± 7	9.4 ± 0.2	46	169	215	817	4.5	0.3
TiO_2	152 ± 1	–	–	–	–	517	3.4	–
MoT	119 ± 2	–	128	110	238	476	4.0	0.5
0.6CoMoT	94 ± 1	5.9 ± 0.1	199	84	283	367	3.9	0.8

a $\frac{H_2 uptake\ (\mu mol\ g^{-1})}{NH_3 uptake\ (\mu mol\ g^{-1})}$.

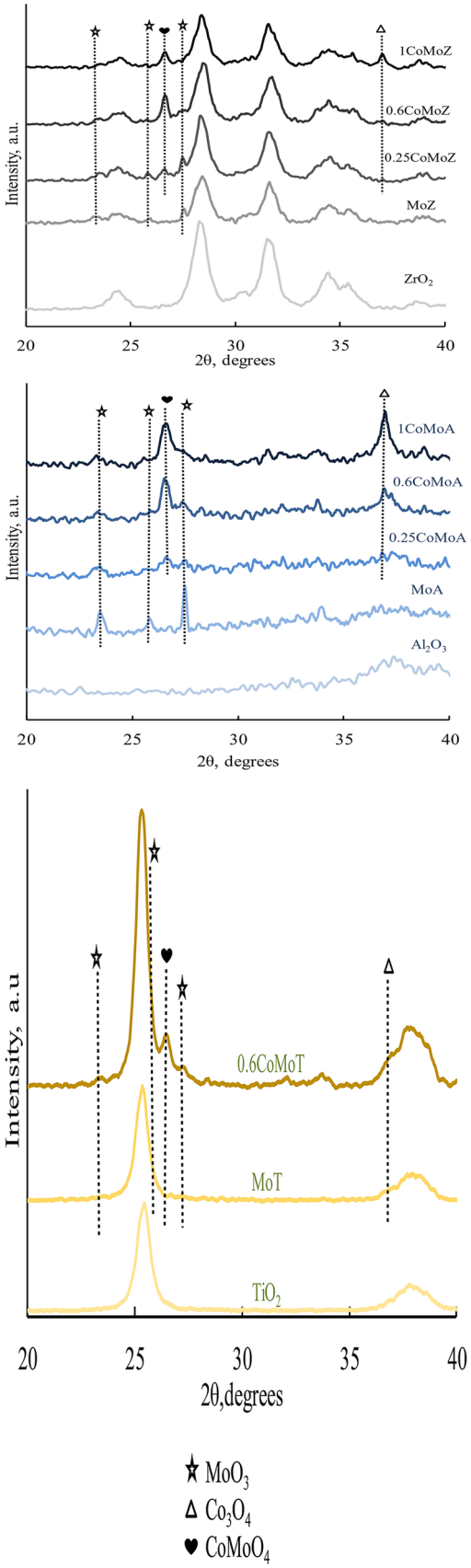

Fig. 1. X-Ray Diffractograms of (a) zirconia (b) alumina and (c) titania supported as prepared calcined materials.

XRD amorphous in the MoT sample, see Fig. 1(c).

3.1.3. Reduction behavior

Fig. 2 depicts the H_2TPR profiles of the supported CoMo oxide samples along with the pure supports. These profiles are interpreted in terms of two stages: the first within a temperature range 300–600 °C (region I), followed by the second one at temperatures exceeding 600 °C (region II). No significant reduction has been observed during pure supports' TPR, see Fig. 2.

Within region I, the first peak, i.e., between 300 and 400 °C, is attributed to the reduction of Co_3O_4 to CoO [46,47]. No such peak is observed on 0.6CoMoT. This, however, may correspond to the high dispersion (as also evident from the XRD measurements, see Fig. 1) and the low reducibility of the Co_3O_4 phase and/or peak overlap with the one corresponding to the reduction of octahedral molybdena (MoO_3) to Mo^{4+} [48]. The second peak, i.e., the one between 430 and 550 °C corresponds to the reduction of octahedrally co-ordinated Mo^{6+} present in MoO_3 and $CoMoO_4$ to Mo^{4+} [32,49]. It is reported that during TPR, Mo^{6+} transforms into Mo^{4+} through an intermediate state (Mo^{5+}) [50], see also Section 3.3 where the surface characterization (XPS) of the reduced material is discussed in more detail. This Mo^{6+} reduction peak shifts to higher reduction temperatures with increasing Co/Mo ratio (see particularly Fig. 2(b) for the alumina support), potentially because the $CoMoO_4$ crystalline phase, which is emerging with the Co content, limits the reducibility of Mo^{6+} [46,51].

Region II reflects the further reduction of the hardly reducible Co and Mo species. The broad peaks around 720–850 °C are ascribed to the reduction of CoO to Co and of tetrahedrally co-ordinated molybdena (MoO_3) to Mo^{4+} [30,47]. The tetrahedral phase of Mo^{6+} is difficult to reduce due to strong metalsupport interactions [32]. The further reduction of Mo^{4+} to Mo^{3+} species could also be associated with this peak [29]. The corresponding hydrogen uptake values are given in Table 2. Interestingly, alumina and zirconia supported CoMo catalysts exhibited higher hydrogen consumption in region II compared to their Mo variants and to titania supported ones, see Table 2.

3.1.4. Acidic properties

Fig. 3 depicts the NH_3-TPD profiles of the supported CoMo oxide samples. The corresponding ammonia uptake values are given in Table 2, showing that the catalysts, in terms of total acidity, are ranked as follows: CoMoA > CoMoT > CoMoZ. The impregnation of the active phase decreased the total acidity of the catalysts compared to their respective bare supports, see Table 2 [52]. The decline in total acid strength could indicate that Co and Mo oxide phase partially covered the acid sites on the supports [52]. Acid site densities expressed as NH_3 uptake per SSA of the catalyst, μmol m^{-2}, were found to be rather similar, yet the metal to acid site ratios vary somewhat more across differently supported catalysts, see Table 2. Through the acidity measurements performed in this work, no distinction could be made between the Lewis (LAS) and Brønsted (BAS) acid sites present on the catalyst materials. However, typically Al_2O_3 and TiO_2 contain both LAS and BAS while ZrO_2 contains predominantly LAS [27,53,54].

As can be observed in Fig. 3, all the catalysts exhibit broad desorption peaks, indicating a wide distribution of acid strength on the surface of the catalysts. Depending on the desorption temperature (T_d), acid sites were designated as: weak, (T_d < 250 °C), medium, (250 < T_d < 450 °C) and strong, (450 °C < T_d). Sites of medium acid strength seem to dominate in the structure of all investigated materials, followed by weakly and strongly acidic sites. In particular, the TPD profiles of the alumina catalysts exhibit a clear tailing behavior at temperatures exceeding 450 °C indicating the presence of some strong acidic sites. Zirconia and titania supported catalysts mainly have weak and medium acidic sites, while strong acidic sites on these materials are negligible.

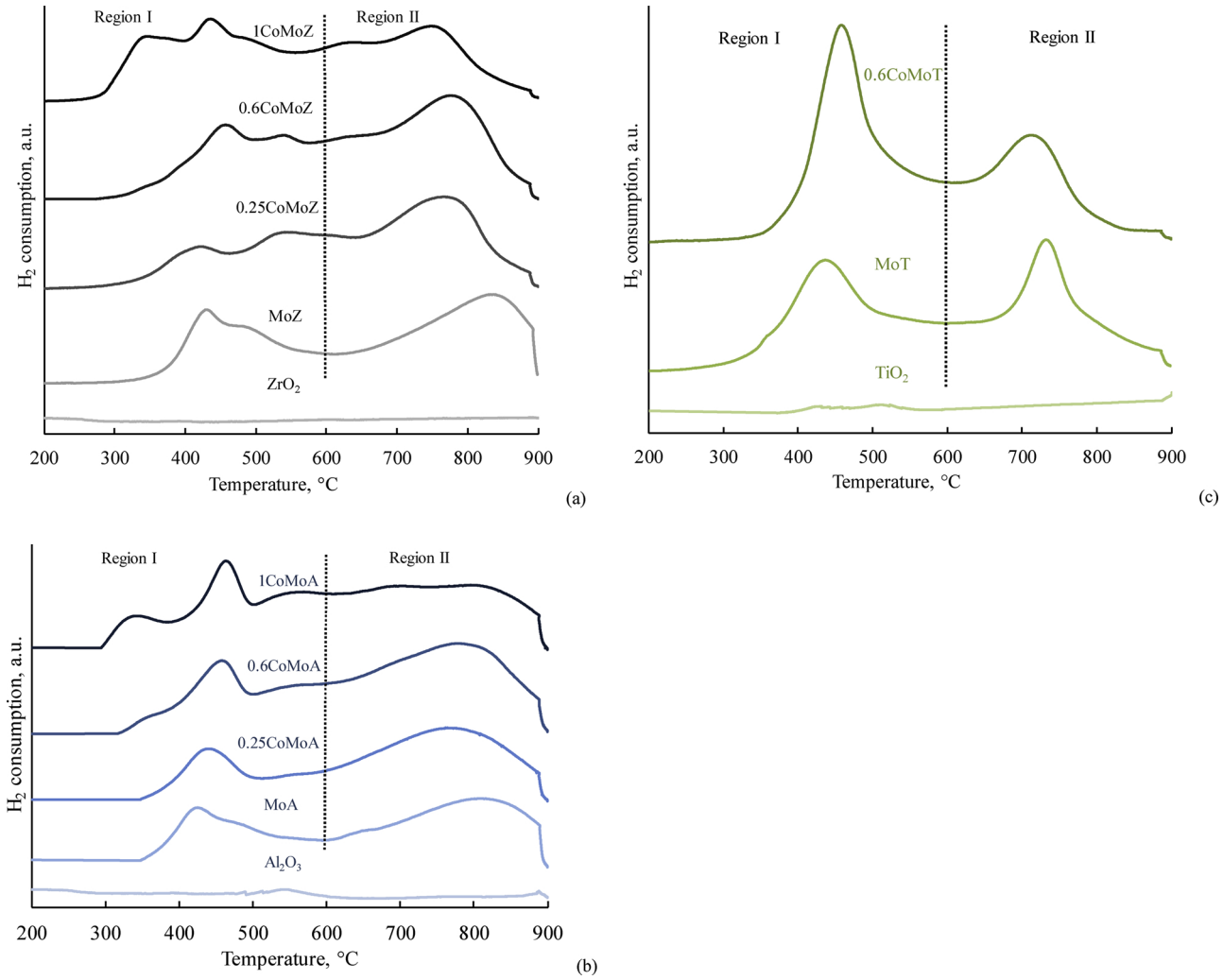

Fig. 2. H_2-Temperature Programmed Reduction (H_2-TPR) of (a) zirconia (b) alumina and (c) titania supported as prepared calcined materials.

3.2. Catalytic performance evaluation

3.2.1. Activity and stability

As relevant conditions for HDO activity testing a reaction temperature and total pressure of 340 °C and 0.5 MPa, respectively were selected [30], employing a H_2 to anisole inlet molar ratio of 50 mol mol^{-1} within a space time between 5–230 kg_{cat} s $mol^{-1}_{anisole}$. In case of zirconia-supported catalysts, tested at a space-time of 128 kg_{cat}s $mol_{anisole}^{-1}$, the activity of the monometallic MoZ decreases during the first 10 h TOS and then remains rather stable up to 50 h TOS, see Fig. 4(a). The bimetallic CoMoZ catalysts with the highest Co/Mo ratio, i.e., 0.6 and 1, exhibited a higher initial activity than MoZ and 0.25CoMoZ. However, the activity of bimetallic CoMoZ materials seems to decrease more significantly during the first 10 h TOS, as compared to MoZ, while their deactivation continued for higher TOS, albeit less steeply.

The alumina supported catalyst series displayed a similar performance in terms of catalyst stability as the zirconia supported ones. As evident from Fig. 4(b), the monometallic MoA material exhibited a less pronounced deactivation than the bimetallic CoMo variants. Overall, however, alumina catalysts exhibited a significantly higher initial anisole conversion, i.e., up to 97%, see SI Fig. 3, in the same space-time range as employed for the zirconia based catalysts. Thus, to generate the intrinsic kinetics character of the data and achieve comparable conversions among the investigated materials, the alumina catalysts were evaluated at a much lower space-time, i.e., 12 kg_{cat} s $mol_{anisole}^{-1}$ (instead of 128 kg_{cat}s $mol_{anisole}^{-1}$ used for zirconia and titania catalysts, see Fig. 4). In terms of activity, titania supported catalysts displayed a comparable level of initial conversions to zirconia supported ones at identical space-time, see Fig. 4(c). In contrast to their zirconia and alumina supported counterparts, Co incorporation into the MoT catalytic system did not significantly impact on the deactivation behavior of the material, yet it decreased the initial activity compared to that of the monometallic MoT, see Fig. 4(c). In the present work, even though catalysts with different supports exhibited similar acid site densities, see Table 2, Section 3.1.4, the differences in strength of these acid sites results in different levels of initial activity per gram of the catalysts [37,53,55]. Alumina supported catalysts with relatively more strong acid sites exhibited higher activity (up to 97% conversion, see SI Fig. 3) in comparison to zirconia and titania supported catalysts, where more weak and medium acid sites are present.

Our previous work on zirconia supported Mo catalysts [30] indicated that the decreasing catalyst activity with time on stream could be, in part, attributed to carbon deposition during the course of the reaction, which decreases the exposure of the catalyst's active phase to the reactants and results in a reduced overall activity [4,29]. The correlation between time on stream performance and catalyst properties is discussed in more detail further in Section 4.

3.2.2. Product selectivity and reaction pathways

The typical product spectrum for all the investigated catalysts contained benzene, phenol, cresol, toluene, xylenes, methyl anisole,

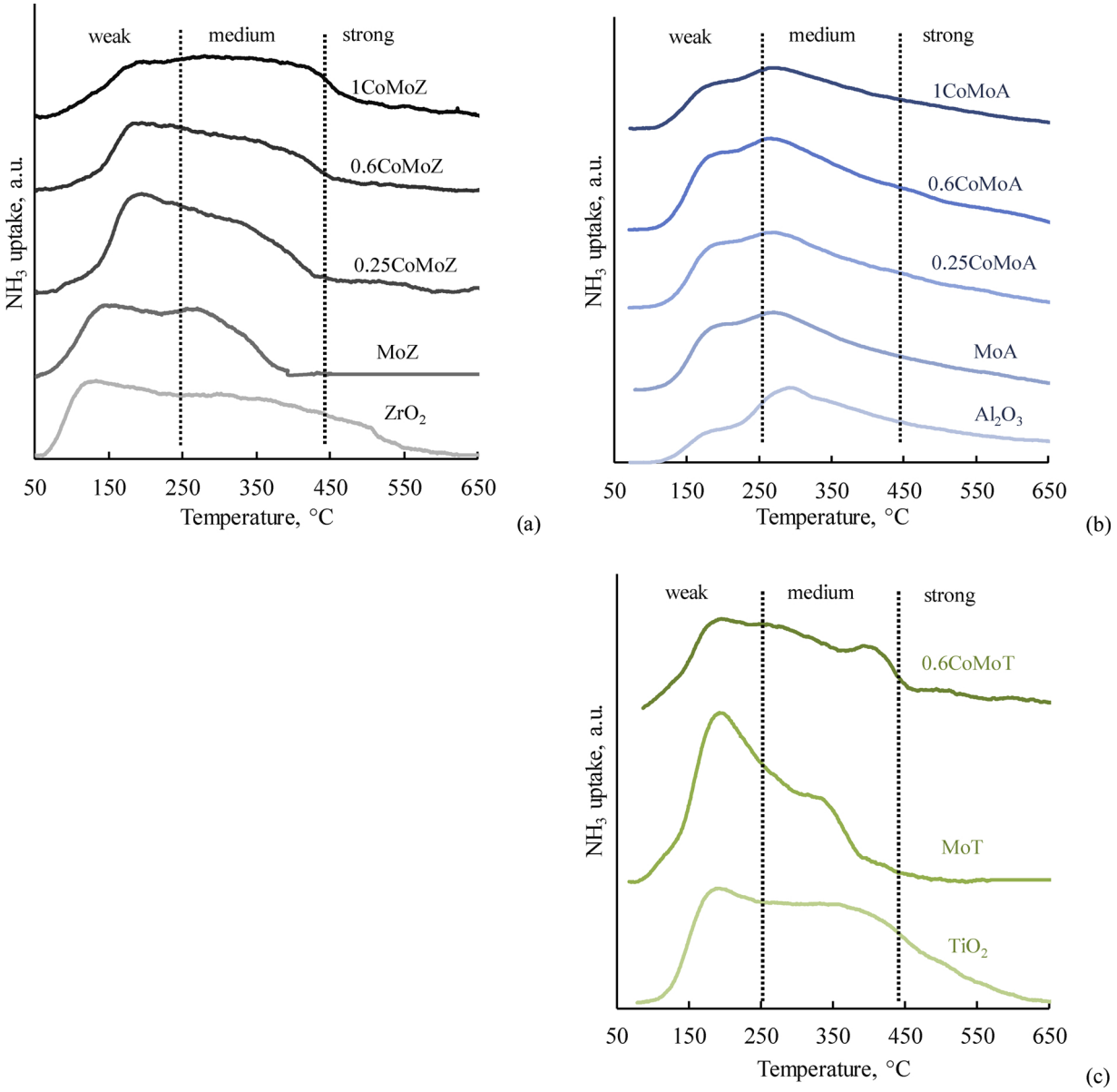

Fig. 3. NH_3-Temperature Programmed Desorption (NH_3-TPD) of (a) zirconia (b) alumina and (c) titania supported as prepared calcined materials.

and dimethyl phenol. Trace amounts of heavier aromatic products such as trimethylbenzenes were also detected. Methane was the only light hydrocarbon by-product observed. The typical mass and carbon balances were closed within 5%. Main product selectivities are displayed in Fig. 5(a) and SI Fig. 4 for bimetallic catalysts, with a Co/Mo ratio of 0.6. For all catalysts, the deoxygenated product selectivity, i.e., towards benzene and toluene, exhibited a decreasing trend with TOS, similar to that observed for the anisole conversion (see Fig. 4), in contrast to the phenolic product selectivity, i.e., phenol, cresol and dimethyl phenol, which increases with TOS. Given the decrease in conversion with TOS, the above-described behavior is in line with what can be expected from a mere conversion effect in a consecutive reaction mechanism [30]. In terms of deoxygenated product selectivity, the investigated materials are ranked as follows: CoMoZ > CoMoT > CoMoA. All materials exhibited a negligible selectivity towards aromatic ring hydrogenation products, under the investigated range of operating conditions.

The acquired data suggest that anisole transformation under the aforementioned HDO conditions over the mono- and bi metallic materials occurs through a complex reaction network, similar to that reported in our previous work over monometallic zirconia supported Mo catalysts [30]. It was also found that, irrespective of the support, CoMo catalysts exhibit higher deoxygenation selectivity, as compared to the monometallic Mo catalysts at iso-conversion, i.e., 30%, see Fig. 5 (b). Incorporation of Co into Mo catalytic system selectively affected the kinetics of the already considered steps and resulted in an enhanced total HDO product (BTX - benzene, toluene, and xylenes) selectivity rather than opening up new reaction pathways. The reaction network that is consistent with our results is presented in Fig. 6.

Anisole conversion on the investigated CoMo catalysts mainly started via the cleavage of the $C_{aliphatic}$– O bond with formation of phenol and methane, i.e., demethylation. Methanol was not observed in the product stream, suggesting that the catalysts preferably cleave $C_{aliphatic}$ – O rather than $C_{aromatic}$ – O bond in anisole HDO [56–58]. The former is, indeed, weaker than the latter as already pointed out in Section 1 [6,19]. Phenol hydrodeoxygenation leads to benzene production. Further, aromatic hydrogenation of benzene to cyclohexene was found to be very limited i.e., selectivity < 1%. The formation of methyl anisole, cresol, and dimethyl phenol also confirms the occurrence of intermolecular and intramolecular methyl group transfer. Cresol and dimethyl phenol were found to further transform into

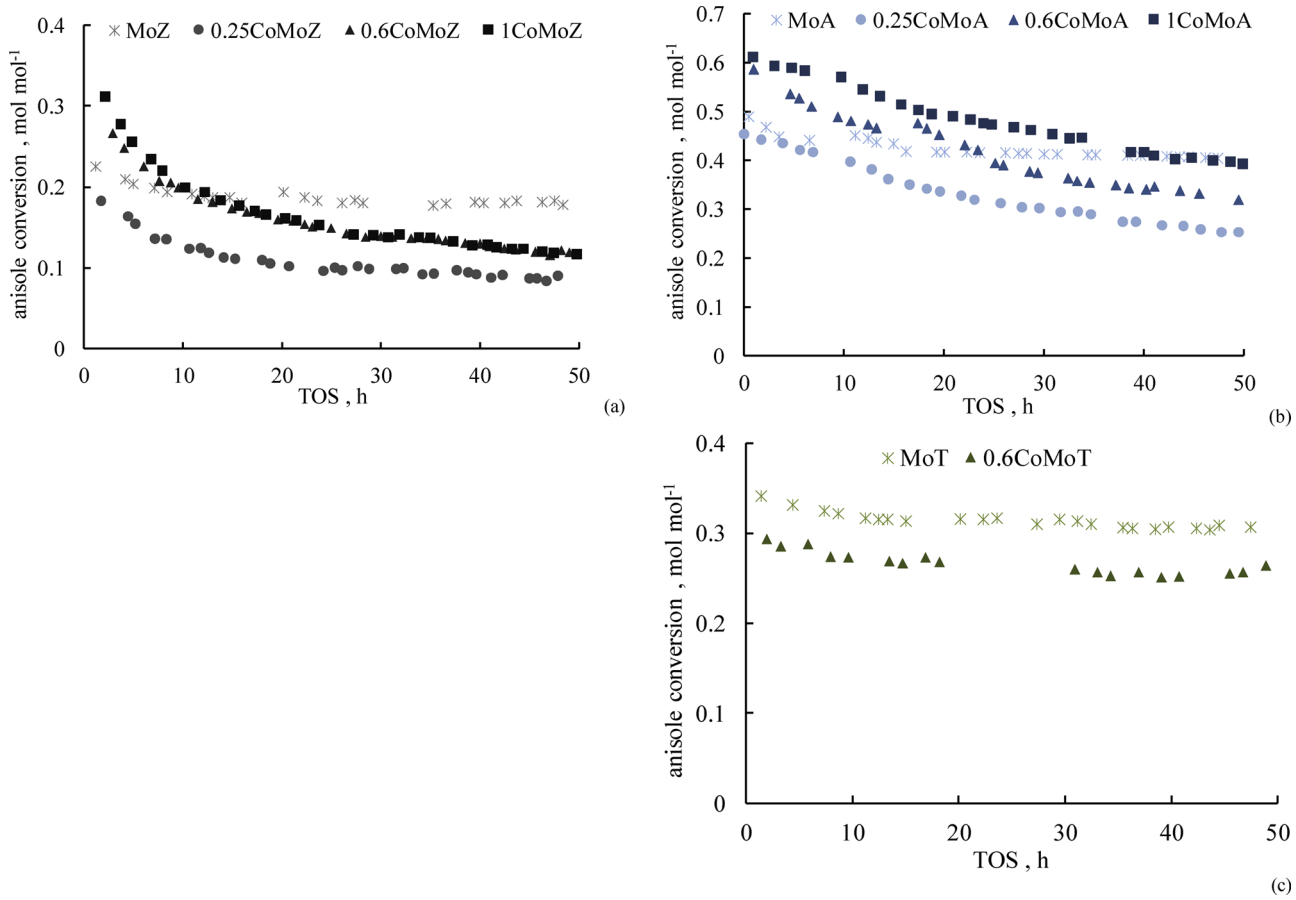

Fig. 4. (a, b, c) Total activity of CoMo catalysts with TOS for zirconia, alumina, and titania supported catalysts respectively. Operating conditions: T = 340 °C, P_T = 0.5 MPa, H_2/anisole = 50 mol mol^{-1}, W/F^o = 128 kg_{cat} s $mol_{anisole}{}^{-1}$ (except for alumina supported catalysts the space-time tested was 12 kg_{cat} s $mol_{anisole}{}^{-1}$).

toluene and xylenes, respectively, through direct hydrogenolysis [59,60]. Furthermore, aromatic ring methylation leading to tri-methylated benzenes was found to take place only to a negligible extent. The introduction of Co into the Mo catalysts greatly enhanced their performance in terms of HDO selectivity through hydrogenolysis of phenolic oxygenates (phenol, cresol, and dimethyl phenol) into alkylated aromatics (benzene, toluene and xylenes). The presence of Co around the active Mo oxide species apparently promotes the breakage of phenolic $C_{aromatic}$ −O bond, e.g., by lowering the activation energy in comparison to an un-promoted Mo catalyst [19,31,61].

Optimal HDO performance has been reported to not only depend on the metal (oxide) but also on the acid strength of the catalyst [4,62]. It is reported that, the acidic site strength of the affects the adsorption of reactants and intermediates, as well as dictates the course of the reaction [4,53,63]. In our work, alumina supported CoMo catalysts, exhibiting the highest acidity among the investigated materials, see Table 2 and Fig. 3, were found to yield more transalkylation rather than deoxygenation products (S_{HDO} = 8%), see Fig. 5. Due to relatively higher amount of strong acid sites on alumina supported (Co)Mo catalysts, the phenol intermediate can dissociate on the support and does not necessarily strongly interact with the active metal phase [17,63]. As a result, phenol and its methylated variants constituted the major product fraction in case of alumina catalysts. In contrast, zirconia supported bimetallic materials with more weak acid sites and lower total acidity, mainly led to deoxygenation reactions, resulting in a S_{HDO} as high as 86%. Benzene constituted the major share (66%) of deoxygenated products with mono-, di-, and traces of tri-methylated benzenes being the rest, on ZrO_2 supported catalysts, see Fig. 5(a). Along with deoxygenated products, zirconia supported catalysts displayed a good amount (selectivity = 10%) of aromatic ring methylation onto anisole resulting in methyl anisole. Titania supported CoMo materials presented medium strength acidity and their selectivities towards transalkylation and deoxygenation products were found to be comparable, i.e., 60 and 40% respectively with benzene and phenol as major part of the product spectrum followed by their methylated derivatives and methyl anisole, see Fig. 5(a).

In comparison to our previous work on zirconia supported Mo catalysts [30], CoMoZ catalysts in this work exhibited 45% higher HDO selectivity. In addition, the present CoMoZ catalysts exhibited higher deoxygenation selectivity (86%) with negligible aromatic ring hydrogenation compared to noble metals such as Ru (50% HDO selectivity at similar hydrogen pressures, 0.5 MPa) [23] and Pt, Pd (up to 60% HDO selectivity at higher hydrogen pressures, 3–4 MPa) [25,26].

3.3. Spent catalyst study

As evident from the results presented above, the catalysts HDO performance in terms of activity, stability and selectivity varies with the incorporation of Co as well as with the selected support. The active sites attributed to Mo are still believed to be the main contributors to the reaction. Yet the catalyst performance is significantly affected by the incorporation of Co and the differences in support *via* changes in reducibility and acidity, mainly.

To gain more insight into the changes that the catalyst structure and the active surface undergo during anisole HDO, both reduced, i.e, prior to testing, and spent, after 50 h TOS testing, catalyst samples were characterized *via* XPS and O_2-TPO. With respect to XPS, emphasis was placed on the high-resolution window of Mo 3d transitions. After deconvolution of the XPS spectra, the contribution of the various Mo species, i.e., Mo^{6+}, Mo^{5+}, Mo^{4+} and Mo^{3+} was determined, see Fig. 7.

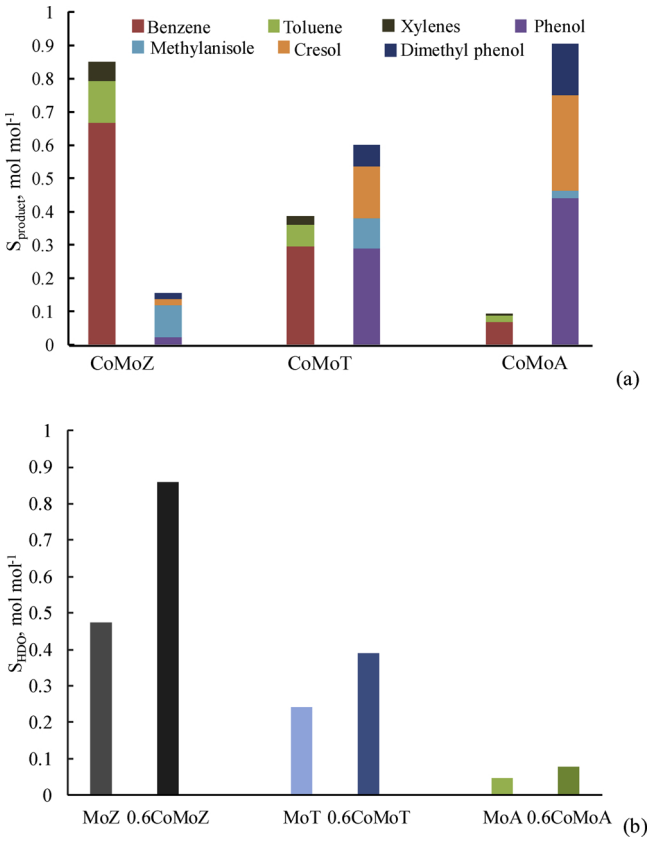

Fig. 5. (a) A comparison of main product selectivity and (b) deoxygenation product selectivity of Mo and CoMo catalysts during anisole HDO (T = 340 °C, P_T = 0.5 MPa, H_2/anisole = 50 mol mol^{-1}, space-time = 5–180 kg_{cat} s mol^{-1}) at iso-conversion (≈30%).

The binding energies of Mo^{6+}, Mo^{5+}, Mo^{4+}, Mo^{3+} species were found to be at 232.0–232.4, 231.0–231.6, 229.1–229.7, and 228.5–228.9 eV respectively, which is consistent with previously reported values [29,41,64,65]. It was found that the reduced catalyst samples still contain the original Mo^{6+} species as well as lower Mo oxidation states, Mo^{5+} and Mo^{4+}, but no Mo^{3+} or metallic Mo phase. The existence of Mo^{5+} and Mo^{4+} species in reduced catalysts indicates the creation of active Mo oxide defects as reported elsewhere [11,12,29,30]. Mo^{3+} was identified only in the spent bimetallic samples CoMoZ and CoMoA. As can be seen from Fig. 7, the incorporation of Co in the zirconia and alumina supported Mo oxide catalysts, facilitates the reduction of Mo^{4+} to Mo^{3+} species during reaction, while it has a negligible effect in the case of titania supported material [66,67]. Easier reducibility of Co species and the electronic interaction between Co and Mo leads to a deeper reduction of Mo species [48]. The differences in deeper reducibility between zirconia, alumina supported catalysts and titania supported one, are attributed to differences in metal support interactions [37]. This finding can also account for the relatively high hydrogen uptake, observed for CoMoZ and CoMoA, during H_2-TPR analysis, in the region (II), compared to their monometallic counterparts and titania supported catalysts, see Table 2 and Fig. 2.

In our previous work, it was found that the presence of Mo^{5+} species was crucial to achieve high catalyst stability and activity, whereas reduction to lower oxidation states induced a negative effect [30]. As can be seen in Fig. 7, the reduced alumina supported monometallic material presents the highest concentration of Mo^{5+}, which is only moderately reduced during HDO testing. This provides an explanation for the relatively high initial activity of MoA and its subsequent stability, see Fig. 4. In addition, the high activity even at lower space-times (see Fig. 4(b)), could be partially attributed to alumina's high acidic strength. However, as mentioned before the incorporation of Co in the supported Mo oxide catalyst leads to steeper deactivation with TOS for MoA and MoZ, whereas it presents no stability effect for MoT, see Fig. 4. This can be ascribed to the over-reduction of the Mo oxides and the formation of Mo^{3+} phase during the anisole HDO testing over MoA and MoZ, see Fig. 7. In contrast, there is no Mo^{3+} phase detected on the surface of the spent MoT sample, but only constrained reduction of Mo^{6+} to Mo^{5+} and Mo^{4+} phases, see Fig. 7. This is probably due to the strong metalsupport interactions in case of titania supported catalysts leading only to a limited reduction under reaction conditions such as anisole HDO [68].

Carbon deposition on the catalyst surface may be another phenomenon responsible for catalyst deactivation with TOS under HDO conditions [29,30]. O_2-TPO was performed on the spent bimetallic materials, with Co/Mo = 0.6, to follow the carbon dioxide evolution as a measure of the nature and quantity of carbonaceous species on the catalyst surface. As can be seen in the corresponding patterns in Fig. 8, MS responses corresponding to CO_2 evolution were identified for all the materials in the temperature range 350–380 °C, indicating the presence of similar carbonaceous deposits, irrespective of the nature of the support. In terms of amount of deposited carbon, see SI Table 4, the investigated materials can be ranked as follows: CoMoA > CoMoT > CoMoZ, identically to the ranking with respect to total acidity, see Table 2 and Fig. 3. The presence of a relatively higher number of strong acid sites in CoMoA induces the formation of a higher amount of coke, which leads to a more pronounced reduction of specific surface area (SSA) and porosity, see SI Table 4, and contributes to the deactivation of the catalytic material, see Fig. 4(b), by covering active sites. Even though CoMoT was found to develop slightly higher amount of coke than CoMoZ, attributed to the relatively higher acidity of the former, it presented a more stable behavior [69]. CoMoZ exhibited a more

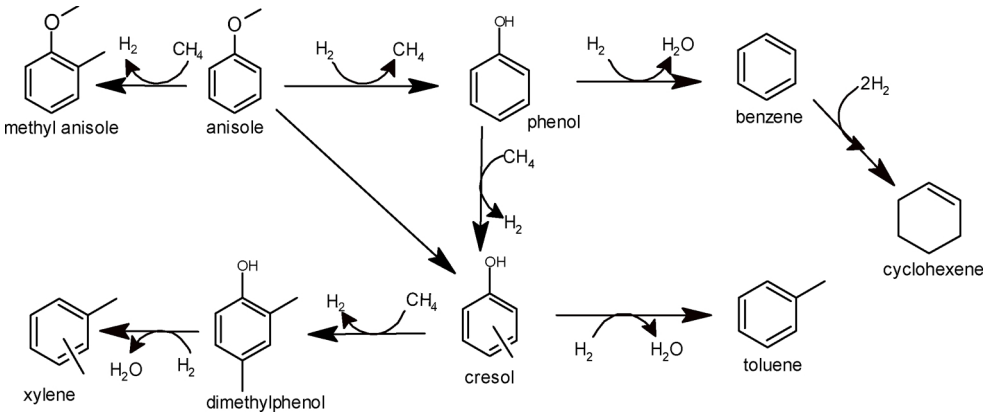

Fig. 6. Proposed anisole HDO reaction pathways.

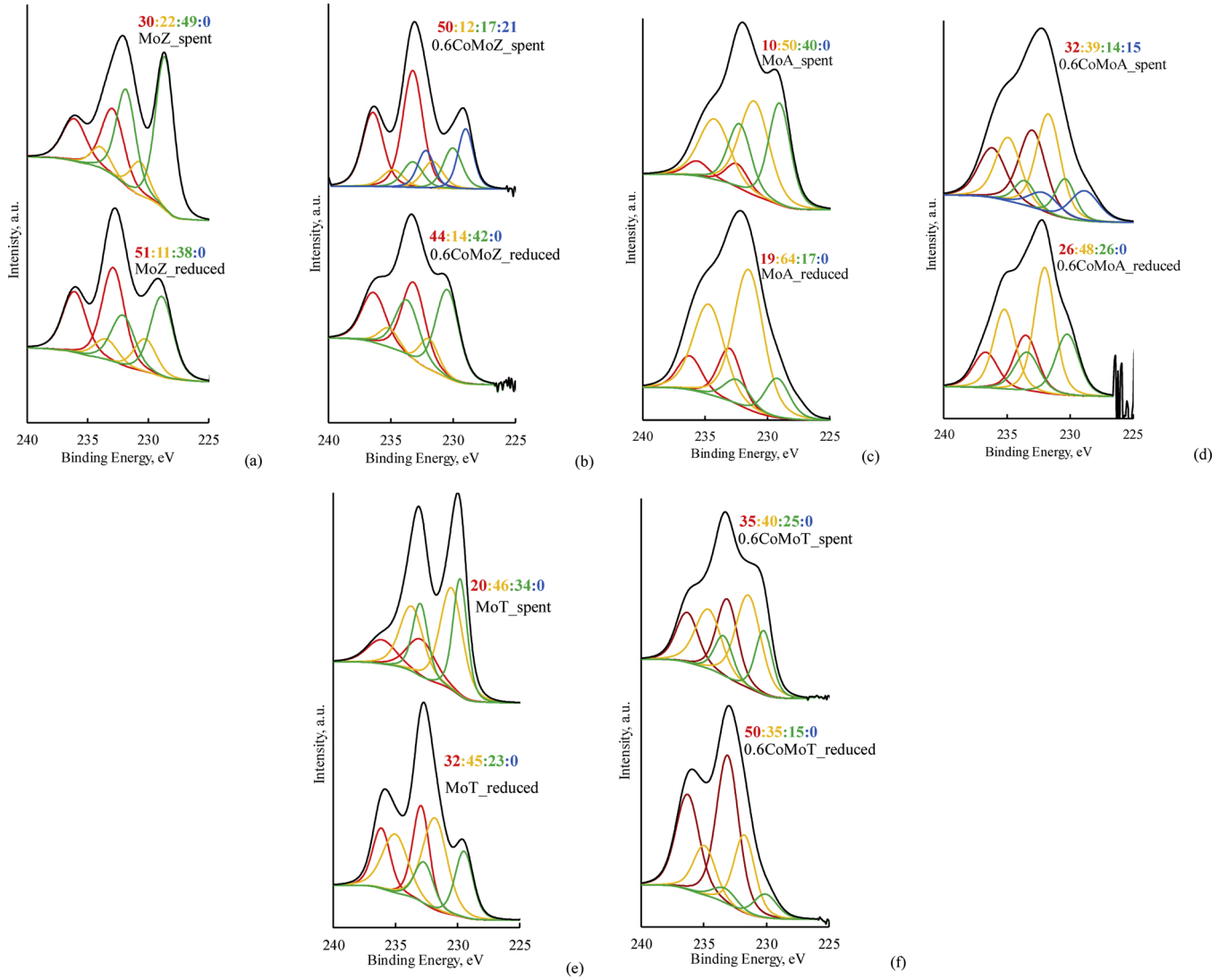

Fig. 7. High-resolution XPS of Mo 3d doublet transitions of catalysts with (a, b) zirconia, (c, d) alumina, and (e, f) titania supports in their reduced and spent form. Red: Mo^{6+}, Orange: Mo^{5+}, Green: Mo^{4+}, Blue: Mo^{3+} (For interpretation of the references to colour in this figure legend, the reader is referred to the web version of this article).

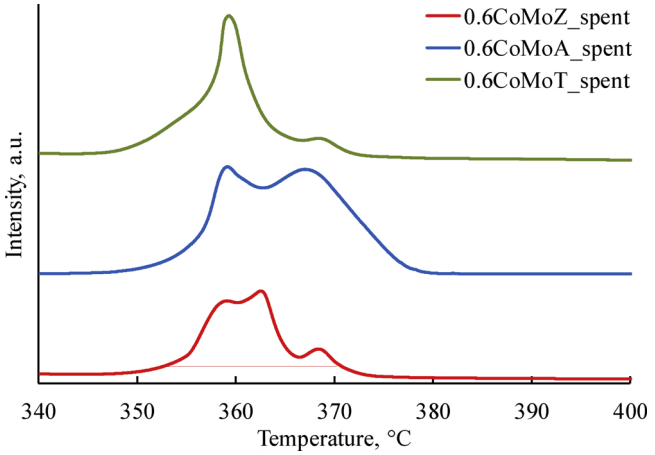

Fig. 8. Evolution of CO_2 (m/z = 44) as a function of temperature for spent catalysts measured by O_2-Temperature Programmed Oxidation (TPO) using MS. Conditions: O_2 in Helium (10% v/v), flow rate = 45 ml min^{-1} Ramp rate = 10 °C min^{-1}. Catalyst mass ≈ 100 mg. Reaction conditions: T = 340 °C, P_T = 0.5 MPa, H_2/anisole = 50 mol mol^{-1}, W/F^o = 12–125 kg_{cat} s $mol_{anisole}^{-1}$, TOS = 50 h.

pronounced deactivation trend under 50 h TOS HDO conditions, see Fig. 4(a, c). This could be assigned mainly, as mentioned above, to the formation of the less active Mo^{3+} phase.

STEM analysis along with EDX elemental mapping has been performed to determine the structural features of CoMo catalysts with Co/Mo ratio of 0.6, prior to and after reaction. The particle size is difficult to estimate as molybdenum is practically homogeneously spread over the support. The structural morphology of the catalyst materials is intact even after 50 h on stream. No evidence of sintering is identified, see SI Fig. 5.

4. Conclusions

The roles of Co incorporation into Mo based catalysts and support properties on catalyst stability and HDO selectivity are correlated to key properties such as reducibility, acidity and metal-support interaction through a wide range of physicochemical analyses of the as prepared, reduced as well as spent catalysts. Titania supported catalysts remain relatively stable over 50 h TOS during anisole HDO as compared to zirconia and alumina supported variants. Bimetallic CoMo catalysts exhibit higher (up to 45%) HDO selectivity than their Mo counterparts within the investigated range of operating conditions. While alumina

supported catalysts displayed higher activity compared to titania and zirconia catalysts, they were mainly selective towards transalkylation (demethylation-methylation) products rather than consecutive deoxygenated products. Whereas, titania supported catalysts exhibited an equivalent selectivity towards transalkylated and deoxygenated products. Zirconia supported catalysts (CoMoZ) presented the highest HDO selectivity (up to 86%) among all others. XPS analyses reinforced Mo^{5+} as the main contributor to the catalysts activity for anisole HDO. Main causes for catalyst deactivation are Mo over-reduction to Mo^{4+} and Mo^{3+} as well as carbonaceous deposits covering the active sites and blocking catalyst pores. The trend in the coke quantity reflects the trend in the acid strength of supports: CoMoA > CoMoT > CoMoZ. In order to improve the catalyst stability, activity, and HDO selectivity, detailed in-situ kinetic studies are needed and will be crucial further in determining the role of various reduced Mo species and acid sites on supported CoMo catalysts for HDO.

Acknowledgments

This work is supported by the Innovative Catalyst Design for large-scale sustainable processes (*i*-CaD) project, which is an ERC consolidator grant, by the European Commission in the 7th Framework Programme (GA no 615456). It also fits in the framework of the FAST industrialization by Catalyst Research and Development (FASTCARD) project, which is a large scale collaborative project supported by European Commission in the 7th Framework Programme (GA no 604277). J.L. is a postdoctoral fellow of the Research Foundation - Flanders (12Z2218N).

Appendix A. Supplementary data

Supplementary material related to this article can be found, in the online version, at doi:https://doi.org/10.1016/j.apcata.2018.12.004.

References

[1] Z. Si, X. Zhang, C. Wang, L. Ma, R. Dong, Catalysts 7 (2017) 169–190.
[2] T.P. Vispute, H. Zhang, A. Sanna, R. Xiao, G.W. Huber, Science 330 (2010) 1222–1227.
[3] T. Dickerson, J. Soria, Energies 6 (2013) 514–538.
[4] M. Saidi, F. Samimi, D. Karimipourfard, T. Nimmanwudipong, B.C. Gates, M.R. Rahimpour, Energy Environ. Sci. 7 (2014) 103–129.
[5] J. Zakzeski, P.C.A. Bruijnincx, A.L. Jongerius, B.M. Weckhuysen, Chem. Rev. 110 (2010) 3552–3599.
[6] E. Furimsky, Appl. Catal. A 199 (2000) 147–190.
[7] H. Wang, J. Male, Y. Wang, ACS Catal. 3 (2013) 1047–1070.
[8] G.W. Huber, S. Iborra, A. Corma, Chem. Rev. 106 (2006) 4044–4098.
[9] S. Jin, Z. Xiao, C. Li, X. Chen, L. Wang, J. Xing, W. Li, C. Liang, Catal. Today 234 (2014) 125–132.
[10] X. Zhang, X. Chen, S. Jin, Z. Peng, C. Liang, ChemistrySelect 1 (2016) 577–584.
[11] T. Prasomsri, T. Nimmanwudipong, Y. Román-Leshkov, Energy Environ. Sci. 6 (2013) 1732–1738.
[12] T. Prasomsri, M. Shetty, K. Murugappan, Y. Román-Leshkov, Energy Environ. Sci. 7 (2014) 2660–2669.
[13] W.-S. Lee, Z. Wang, R.J. Wu, A. Bhan, J. Catal. 319 (2014) 44–53.
[14] S. Jin, Z. Xiao, X. Chen, L. Wang, J. Guo, M. Zhang, C. Liang, Ind. Eng. Chem. Res. 54 (2015) 2302–2310.
[15] S. Jin, X. Chen, C. Li, C.W. Tsang, G. Lafaye, C. Liang, ChemistrySelect 1 (2016) 4949–4956.
[16] D.C. Elliott, Energy Fuels 21 (2007) 1792–1815.
[17] A. Popov, E. Kondratieva, L. Mariey, J.M. Goupil, J. El Fallah, J.-P. Gilson, A. Travert, F. Maugé, J. Catal. 297 (2013) 176–186.
[18] M. Badawi, J.F. Paul, S. Cristol, E. Payen, Y. Romero, F. Richard, S. Brunet, D. Lambert, X. Portier, A. Popov, J. Catal. 282 (2011) 155–164.
[19] V.N. Bui, D. Laurenti, P. Afanasiev, C. Geantet, Appl. Catal. B 101 (2011) 239–245.
[20] N.T. Tran, Y. Uemura, S. Chowdhury, A. Ramli, Appl. Catal. A 512 (2016) 93–100.
[21] T.M. Sankaranarayanan, A. Berenguer, C. Ochoa-Hernandez, I. Moreno, P. Jana, J.M. Coronado, D.P. Serrano, P. Pizarro, Catal. Today 243 (2015) 163–172.
[22] I.D. Mora-Vergara, L.H. Moscoso, E.M. Gaigneaux, S.A. Giraldo, V.G. Baldovino-Medrano, Catal. Today 302 (2018) 125–135.
[23] T.N. Phan, Y.-K. Park, I.-G. Lee, C.H. Ko, Appl. Catal. A 544 (2017) 84–93.
[24] M. Lu, H. Du, B. Wei, J. Zhu, M. Li, Y. Shan, J. Shen, C. Song, Ind. Eng. Chem. Res. 56 (2017) 12070–12079.
[25] L. Wang, H. Wan, S. Jin, X. Chen, C. Li, C. Liang, Catal. Sci. & Technol. 5 (2015) 465–474.
[26] L. Wang, C. Li, S. Jin, W. Li, C. Liang, Catal. Lett. 144 (2014) 809–816.
[27] P.M. de Souza, R.C. Rabelo-Neto, L.E. Borges, G. Jacobs, B.H. Davis, T. Sooknoi, D.E. Resasco, F.B. Noronha, ACS Catal. 5 (2015) 1318–1329.
[28] Z. He, M. Hu, X. Wang, Catal. Today 302 (2018) 136–145.
[29] M. Shetty, K. Murugappan, T. Prasomsri, W.H. Green, Y. Román-Leshkov, J. Catal. 331 (2015) 86–97.
[30] C. Ranga, R. Lødeng, V.I. Alexiadis, T. Rajkhowa, H. Bjørkan, S. Chytil, I.H. Svenum, J. Walmsley, C. Detavernier, H. Poelman, J.W. Thybaut, Chem. Eng. J. 335 (2018) 120–132.
[31] J. Shabtai, N. Nag, F. Massoth, J. Catal. 104 (1987) 413–423.
[32] K.V.R. Chary, K.R. Reddy, G. Kishan, J.W. Niemantsverdriet, G. Mestl, J. Catal. 226 (2004) 283–291.
[33] E.A. El-Sharkawy, A.S. Khder, A.I. Ahmed, Microporous Mesoporous Mater. 102 (2007) 128–137.
[34] B. Wang, G. Ding, Y. Shang, J. Lv, H. Wang, E. Wang, Z. Li, X. Maa, S. Qin, Q. Sun, Appl. Catal., A 431-432 (2012) 144–150.
[35] K.D. Chen, S.B. Xie, E. Iglesia, A.T. Bell, J. Catal. 189 (2000) 421–430.
[36] S. Xie, K. Chen, A.T. Bell, E. Iglesia, J. Phys. Chem. B 104 (2000) 10059–10068.
[37] O. Valdés-Martínez, V. Suárez-Toriello, J. de los Reyes, B. Pawelec, J. Fierro, Catal. Today 296 (2017) 219–227.
[38] K. Van der Borght, V.V. Galvita, G.B. Marin, Appl. Catal., A 492 (2015) 117–126.
[39] J.E. De Vries, H.C. Yao, R.J. Baird, H.S. Gandhi, J. Catal. 84 (1983) 8–14.
[40] M.J. Ledoux, C. Pham-Huu, H. Dunlop, J. Guille, J. Catal. 134 (1992) 383–398.
[41] J.G. Choi, L.T. Thompson, Appl. Surf. Sci. 93 (1996) 143–149.
[42] K. Van der Borght, K. Toch, V.V. Galvita, J.W. Thybaut, G.B. Marin, Catalysts 5 (2015) 1948–1968.
[43] R.J. Berger, E.H. Stitt, G.B. Marin, F. Kapteijn, J.A. Moulijn, Cattech 5 (2001) 36–60.
[44] K.V.R. Chary, G. Kishan, T. Bhaskar, H. Sivaraj, J. Phys. Chem. B 102 (1998) 6792–6798.
[45] K.V.R. Chary, T. Bhaskar, G. Kishan, K.R. Reddy, J. Phys. Chem. B 105 (2001) 4392–4399.
[46] R. Nava, B. Pawelec, P. Castaño, M. Álvarez-Galván, C. Loricera, J. Fierro, Appl. Catal., B 92 (2009) 154–167.
[47] H. Song, L. Zhang, U.S. Ozkan, Green Chem. 9 (2007) 686–694.
[48] C.-M. Wang, T.-C. Tsai, I. Wang, J. Catal. 262 (2009) 206–214.
[49] T. Bhaskar, K.R. Reddy, P.C. Kumar, M.R.V.S. Murthy, K.V.R. Chary, Appl. Catal., A 211 (2001) 189–201.
[50] T. Ressler, R.E. Jentoft, J. Wienold, M.M. Günter, O. Timpe, J. Phys. Chem. B 104 (2000) 6360–6370.
[51] J.E. Herrera, D.E. Resasco, J. Catal. 221 (2004) 354–364.
[52] J. Tavizón-Pozos, V. Suárez-Toriello, P. del Ángel, J. de los Reyes, Int. J. Chem. React. Eng. 14 (2016) 1211–1223.
[53] I. Ghampson, C. Sepúlveda, A. Dongil, G. Pecchi, R. Garcia, J. Fierro, N. Escalona, Catal. Sci. Technol. 6 (2016) 7289–7306.
[54] J.L.G. Fierro, CRC press, Boca Raton, Metal Oxides: Chemistry and Applications, first ed., (2005).
[55] V.N. Bui, D. Laurenti, P. Delichère, C. Geantet, Appl. Catal. B 101 (2011) 246–255.
[56] J.E. Peters, J.R. Carpenter, D.C. Dayton, Energy Fuels 29 (2015) 909–916.
[57] Kelun Li, Rijie Wang, J. Chen, Energy Fuels 25 (2011) 854–863.
[58] D. Otyuskaya, J.W. Thybaut, R. Lødeng, G.B. Marin, Energy Fuels 31 (2017) 7082–7092.
[59] X. Xu, E. Jiang, Z. Li, Y. Sun, Fuel 221 (2018) 440–446.
[60] T.-R. Viljava, R. Komulainen, A. Krause, Catal. Today 60 (2000) 83–92.
[61] M. Badawi, J.F. Paul, E. Payen, Y. Romero, F. Richard, S. Brunet, A. Popov, E. Kondratieva, J.P. Gilson, L. Mariey, Oil Gas Sci. Technol. - Rev. IFP Energies Nouvelles 68 (2013), pp. 829–840.
[62] X. Zhu, L.L. Lobban, R.G. Mallinson, D.E. Resasco, J. Catal. 281 (2011) 21–29.
[63] A. Popov, E. Kondratieva, J.-P. Gilson, L. Mariey, A. Travert, F. Maugé, Catal. Today 172 (2011) 132–135.
[64] D.O. Scanlon, G.W. Watson, D. Payne, G. Atkinson, R. Egdell, D. Law, J. Phys. Chem. C 114 (2010) 4636–4645.
[65] J. Baltrusaitis, B. Mendoza-Sanchez, V. Fernandez, R. Veenstra, N. Dukstiene, A. Roberts, N. Fairley, Appl. Surf. Sci. 326 (2015) 151–161.
[66] M. Ferrari, B. Delmon, P. Grange, Carbon 40 (2002) 497–511.
[67] M. Ferrari, B. Delmon, P. Grange, Microporous Mesoporous Mater. 56 (2002) 279–290.
[68] A.N. Desikan, L. Huang, S.T. Oyama, J. Chem. Soc, Faraday Trans. 88 (1992) 3357–3365.
[69] J. Wildschut, F.H. Mahfud, R.H. Venderbosch, H.J. Heeres, Ind. Eng. Chem. Res. 48 (2009) 10324–10334.